Int. J. Electrochem. Sci., 7 **(2012)** 7587 - 7599

International Journal of
ELECTROCHEMICAL
SCIENCE
www.electrochemsci.org

Preparation and Capacitive Properties of Nitrogen-Enriched Hierarchical Porous Carbon

Chang Ma[1, 2], *Jingli Shi*[1, 3,*], *Yan Song*[1, *], *Dongqing Zhang*[1], *Xiaoling Zhai*[1, 2], *Ming Zhong*[1, 2], *Quangui Guo*[1], *Lang Liu*[1]

[1] Key Laboratory of Carbon Materials, Institution of Coal Chemistry, Chinese Academy of Sciences, Taiyuan 030001, China
[2] Graduate University of Chinese Academy of Sciences, Beijing 100049, China
[3] School of Material Science and Engineering, Tianjin Polytechnic University, Tianjin 300160,China
[*]E-mail: shijingli1963@163.com; yansong1026@126.com

Received: 29 June 2012 / *Accepted:* 18 July 2012 / *Published:* 1 August 2012

Nitrogen-enriched hierarchical porous carbon was prepared from melamine-formaldehyde resin/poly (vinyl alcohol) blend using MgO as template. The structural properties and surface chemistry were characterized by nitrogen sorption at 77 K, transmission electron microscopy and X-ray photoelectron spectroscopy. The results showed that the obtained carbon possessed unique hierarchical porous structure (micropores with the size of ca. 0.85 and 1.76 nm, mesopores with the size of ca. 2.3, 9 and 50 nm, and macropores at 100~200 nm), high meso/macro-porosity (67.3~84.9%) and rich heteroatoms (5.76~9.32 wt.% of N and 10.97~19.66 wt.% of O). Both of the porous structure and surface chemistry could be controlled by adjusting the content of template. The electrochemical performance was investigated by cyclic voltammetry, galvanostatic charge/discharge and impedance spectroscopy in 6M KOH. Analysis revealed that the surface functionalities could greatly enhance the specific surface capacitance and high meso/macro-porosity ensured high rate performance. Dou to the highest meso/macro-porosity (84.9%) and high content of heteroatoms (7.32 wt.% of N and 10.97 wt.% of O), the sample MPM-2 showed superior electrochemical performance (specific capacitance of 224 F g^{-1}, capacitance retention of 67% and specific surface capacitance of 0.64 F m^{-2}).

Keywords: Nitrogen-enriched carbon; Hierarchical pore; MgO template; Melamine; Supercapacitor.

1. INTRODUCTION

Electrochemical double layer capacitors, also known as supercapacitors, can be applied in many fields due to high power density and long cycle life [1]. Such capacitors store energy through charge accommodation at the electrode/electrolyte interface and faradaic reactions [2]. To fabricate high-performance supercapacitors, great efforts have been made to study possible electrode materials.

Among various electrode materials for supercapacitors, porous carbon materials are often regarded as the first candidate, because of their excellent physicochemical stability, high electrical conductivity, relatively low cost, and availability [3, 4].

Activated carbon, a typical microporous carbon, is the most commonly used materials in supercapacitors due to large surface area [4]. However, microporous carbons always suffer from electrode kinetic problems that are related to inner-pore ion transportation. Thus, surface area of micropores cannot be utilized efficiently, resulting in unsatisfactory capacitance and poor rate performance [5]. Hierarchical porous carbons with a certain amount of mesopores and macropores have been strongly recommended to improve ion transportation and rate performance, of which the macropores serve as ion-buffering reservoirs and the mesopores provide a convention ion transportation pathway [6-9]. Recently, several research efforts have been devoted to design and construct such hierarchical porous carbons as electrode materials for supercapacitors. Silica/zeolite template combined with post activation strategy has been widely used [10, 11]. However, this strategy involves expensive template, tedious process and dangerous template-removing procedure. Hence, a low-cost, simplified and environmental-friendly strategy to hierarchical porous carbons is still needed.

Also, due to presence of meso/macropores, the hierarchical porous carbons always present a moderate electrochemical accessible surface area. As a result, high rate performance is always achieved at the expense of satisfactory capacitance. An effective approach to improve the capacitive performance is to introduce heteroatoms, which could provide pseudocapacitance contribution. In the last decade, nitrogen-enriched carbons have been extensively investigated as electrode materials of supercapacitors due to their excellent pseudocapacitance effect [3, 12-16]. However, to the best of our knowledge, there are still few reports about hierarchical porous carbons with enriched nitrogens for supercapacitors.

In this work, we prepare hierarchical porous carbons with enriched nitrogens using melamine-formaldehyde resin (MF)/poly (vinyl alcohol) (PVA) blend as precursor and MgO as template. MF was selected as both carbon source and nitrogen source due to its extra high nitrogen content (48 wt.%) [17]. Enriched nitrogens together with enormous quantities of oxygens were successfully introduced into resultant carbons. Combination of template approach and polymer blending strategy leads to resultant carbons with hierarchical porous structure. Compared with previously-reported pore-forming method, such as silica template combined with post-activation strategy, this way is low-cost, simple, time-saving and safe. The hierarchical porous structure provides the resultant carbons with a fast ion transportation, leading to good rate performance, and enriched nitrogens and oxygens provide considerable pseudocapacitance, which results in a high surface capacitance.

2. EXPERIMENTAL

2.1. Preparation of MPM

First, MF/PVA blend solution was synthesized by formaldehyde (37% wt.% aqueous solution), melamine (A.R.) and PVA (1750±50) with NaOH as catalyst. In the polymerization process, PVA

serves as reaction buffer to aviod fast gelling. Firstly, 12 wt.% PVA aqueous solution was prepared. In the typical experiment, the mixture of 7.37 g melamine, 105 g PVA 12 wt.% aqueous solution, 13.4 g H_2O and 0.1 g NaOH was slowly heated to 75 °C under stirring. Subsequently, 14.22 g formaldehyde was added. The reaction was kept under 75 °C for 1 h, then ceased by cooling down quickly. In the as-synthesized solution, the concentration of MF/PVA is 18 wt.% and mass ratio of MF/PVA is 1:1. Before adding magnesium acetate ($Mg(AC)_2$), the as-synthesized solution was diluted to 9 wt.% in the concentration of MF/PVA and the PH was adjusted to 6 using acetate acid. Then, the $Mg(AC)_2$, in the form of $Mg(AC)_2$ aqueous, was added into MF/PVA aqueous solution under stirring. The mass ratio of the $Mg(AC)_2$/(MF+PVA) (R_{MM}) was controlled to be 1:2, 1:1, 2:1 and 4:1 by varying the amount of $Mg(AC)_2$. The obtained mixed solution was dried at 100 °C and then stabilized at 200 °C for 4 h in air. Carbonization was performed at 750 °C for 1h under flowing nitrogen with heating rate of 3 °C min^{-1}. $Mg(AC)_2$ turns to MgO during carbonization. The obtained C/MgO composites were ground into powder and then treated with excessive 2 M HCl solution. Finally, the mixture was filtered, washed with distilled water until the PH of filtrate is 7, and dried at 100 °C for 12 h to get the porous carbons, which were labeled as MPM-R_{MM} (R_{MM}=0.5, 1, 2, 4.)

2.2. Structural characterization

TEM measurements of MPM-R_{MM}s were performed by transmission electron microscopy (TEM, FEI Tecnai G2 T20 microscopes). The X-ray photoelectron spectroscopy (XPS) measurements were conducted on ESCALAB 250 spectrometer with an Al Kα monochromatic source (150 W, 500 um) and a multidetection analyzer. The porous texture was characterized by physical adsorption of N_2 at 77 K using an automatic adsorption system (ASAP2020, Micromeritics). The samples were previously outgassed at 300 °C for 10 h. The BET surface area (S_{BET}) was analyzed by Brunauer-Emmett-Teller (BET) theory. The total pore volume (V_{tot}) was estimated from single point adsorption at a relative pressure P/P_0 of 0.995. The micropore volume (V_{mic}) was determined by t-plot theory and the sum of mesopore and macropore volume ($V_{(me+ma)}$) was obtained by subtracting V_{mic} from V_{tot}. The pore size distribution (PSD) was analyzed by density functional theory (DFT) and BJH method. Average pore width (D_{av}) was calculated by the BET method (4V/A by BET).

2.3. Electrochemical measurements

The electrochemical measurements were carried out in 6 M KOH using a three-electrode system in CHI 660C instruments (Shanghai Chenhua Apparatus Co. Ltd) at room temperature. Platinum plate and Hg/HgO were used as the counter electrode and the reference electrode, respectively. The working electrode was prepared as follows: firstly, the homogeneous mixture of porous carbon materials (80 wt.%), conductive graphite (10 wt.%) and polytetrafluoroethylene (PTFE) binder (10 wt.%) was pressed into a flake; secondly, the flake was dried overnight at 373 K; finally, the dried flake was mechanically pressed on nickel foam under a pressure of 10 MPa as working electrode. Before electrochemical tests, the working electrodes were impregnated within electrolyte for

24 h to ensure thorough wetting. The cyclic voltammetry (CV) measurements were conducted at different scan rates ranging from 5 to 100 mV s^{-1}. Electrochemical impedance spectroscopy was recorded from 100 kHz to 10 mHz with current amplitude of 5 mV. Galvanostatic charge/discharge measurements were performed at various current densities from 50 to 1000 mA g^{-1}. The potential window used in CV and charge/discharge measurements is -0.9~0 V *vs.* Hg/HgO. Based on the galvanostatic charge/discharge measurement, specific capacitance was calculated according to the equation:

$$C= it/m\Delta V \quad (1)$$

where C is the specific capacitance of the active material (F g^{-1}), i is the discharge current (A), t is the discharge time (s), m is the mass of the electroactive material in the electrode (g) and ΔV is the potential window (V).

3. RESULTS AND DISCUSSION

3.1. Structural and textural properties of Samples

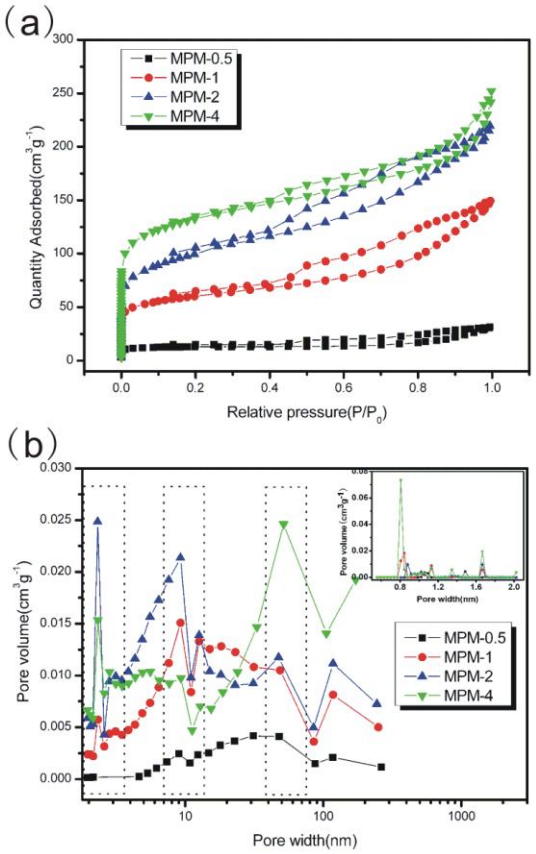

Figure 1. (a) Nitrogen adsorption/desorption isotherms at 77 K of samples and (b) their corresponding pore size distributions.

Nitrogen adsorption was used to examine the changes of the porous characteristics for the resultant carbons. Fig. 1a shows the N_2 adsorption-desorption isotherms of the as-prepared carbons. For all samples, three typical regions in the isotherms can be seen. The distinct capillary condensation step occurs at relative pressure (P/P_0) range of 0.4~1.0, showing typical type IV isotherms with well-defined H4 hysteresis loops, characteristic of mesoporous structure. The steep increase of adsorption amount at low relative pressure and no adsorption plateau at relative pressure near 1.0 suggest the formation of micropores and macropores.

Fig.1b shows PSD of samples in meso-macropore region calculated by BJH method and the inset shows their PSD in micropore region calculated using DFT model. The hierarchical porous structure is apparent since the pores of samples can be divided into three major regions: (1) micropores (<2 nm) with a notable peak at 0.85 and 1.67 nm; (2) hierarchical mesopores (2~50 nm) with a maximum peak at 2.3, 9 and 50 nm; (3) macropores with pore size ranging from 100 to 200nm. Micropores are mainly produced by escape of pyrolysis gas and macropores might result from loose aggregation of carbon nanoparticles. The hierarchical mesopores are supposed to come from MgO template. Different degree of aggregation of MgO particle leads to mesopores with different sizes. The poor thermal stability of PVA prompts the aggregation of MgO particle and collapse of carbon skeleton, leading to bigger mesopores. The possible formation mechanism is displayed in Fig. 2. Pore Ⅰ, Ⅱ and Ⅲ correspond to 2.3, 9 and 50 nm wide pores, respectively. The hierarchical porous structure can be also observed from the TEM images (as seen in Fig. 3). It can be seen that numerous of mesopores with various sizes are scattered in the bulk of carbon, some of which connect to each other and some of which are connected by micropores or macropores, to form a porous network, which provides a convenient ion transportation path.

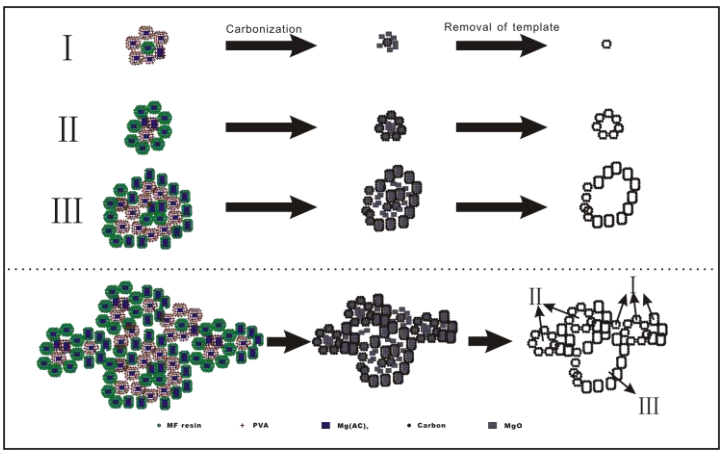

Figure 2. Schematic illustration for the possible formation of the mesopores with different pore sizes. The pore Ⅰ, pore Ⅱ and pore Ⅲ correspond to 2.3, 9 and 50 nm wide pores, respectively.

With the R_{MM} increasing from 0.5 to 2, the pores centered at ca. 2.3 and 9 nm increases gradually, while the pores centered at ca. 50 nm stay unchanged. It suggests that the $Mg(AC)_2$ principally introduces mesopores at ca. 2.3 and 9 nm. However, as the R_{MM} increases from 2 to 4, the

pores at ca. 2.3 and 9 nm shows a distinct decrease while the pores at ca. 50 nm increases a lot, demonstrating that the further increase of R_{MM} leads to drastic aggregation of the MgO particles.

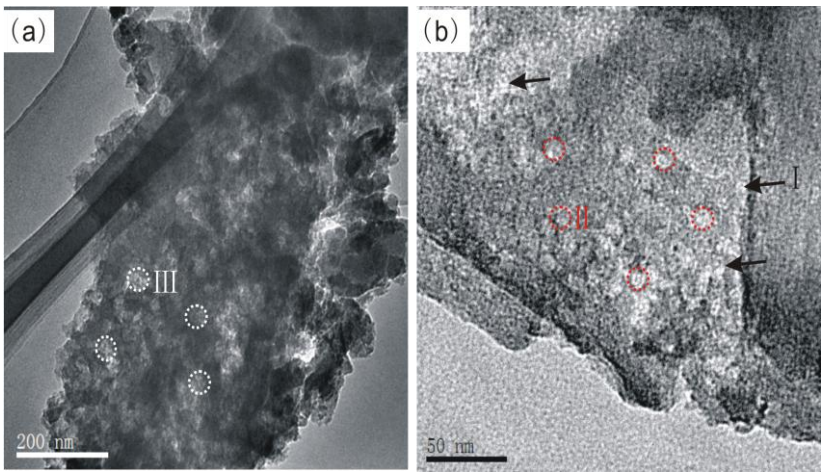

Figure 3. TEM images of MPM-1 at different magnifications. The pore Ⅰ, pore Ⅱ and pore Ⅲ correspond to mesopores with different pore sizes.

Table 1 shows structural parameters of the as-prepared samples. With the increase of R_{MM}, both the pore volume and BET surface area increase gradually. MPM-4 shows the highest BET surface area of 458 m^2 g^{-1}, which is comparable with previously-reported value of MF-based porous carbons (403 m^2 g^{-1} for MF/nanotube composite carbon [18], 86 m^2 g^{-1} for MF/mica based carbon [19], 109~539 m^2 g^{-1} for MF/surfactant based carbon [19]). Different from trimethylolmelamine-based carbon (about 130 m^2 g^{-1} for sample carbonized at 750 °C) [20], MPM-4 possesses much higher surface area and hierarchical porous structure with high meso/macro-porosity (69.4%). It may be attributed to thermosetting resin/thermoplastic polymer mixed precursor, in which thermosetting resin develops into carbon skeleton and thermoplastic polymer produces more pores. With the highest meso/macropore volume of 0.288 ml g^{-1}, MPM-2 possesses meso/macro-porosity as high as 84.9%. Compared with MPM-2, MPM-4 displays a slightly-decreased meso/macropore volume of 0.277 ml g^{-1} and smaller meso/macro-porosity of 69.4%. Being of mesoporous characteristics, all samples present average pore size at 3.4~4.4 nm.

Table 1. Structural characteristics of samples

Sample	S_{BET} (m^2 g^{-1})	V_{tot} (ml g^{-1})	V_{mic} (ml g^{-1})	$V_{(me+ma)}$ (ml g^{-1})	$V_{(me+ma)}/V_{tot}$ (%)	D_{av} (nm)
MPM-0.5	44	0.049	0.016	0.033	67.3	4.40
MPM-1	209	0.231	0.048	0.183	79.2	4.42
MPM-2	349	0.339	0.051	0.288	84.9	3.88
MPM-4	458	0.390	0.113	0.277	69.4	3.41

XPS analysis was performed to study the surface chemical composition of all samples. The relative amounts of carbon, oxygen and nitrogen on the surface are summarized in Table 2. It can be seen that all MPMs have considerable nitrogen content (5.76~9.32 wt.%). Furthermore, it is interesting to note that all MPMs show relatively high oxygen content (10.97~19.66 wt.%), which is higher than most of reported MF-based carbon [19, 21]. It is believed that the PVA plays an active role in increasing oxygen content. It is obvious that R_{MM} makes a distinct influence on the surface chemistry since both nitrogen and oxygen are reduced with the increase of R_{MM}. There is a tendency that the content of nitrogen or oxygen decreases with the increase of S_{BET}. The trend is in agreement with the researches [12, 22]. It may be explained by porosity, which affects the escape of nitrogen- or oxygen-containing gas. The higher porosity provides a more convenient path for the escape of the pyrolysis gas, most of which is the nitrogen- or oxygen-containing gas. Therefore, more nitrogens and oxygens escape out of the carbon bulk before reaction with carbon, namely less nitrogens and oxygens are retained.

Table 2 XPS elemental composition and mass percentages of the different nitrogen or oxygen functionalities.

Sample	wt. %									
	C	N	O	N5	N6	NQ	NX	OI	OII	OIII
MPM-0.5	71.02	9.32	19.66	3.22	3.77	1.77	0.56	2.74	11.95	4.99
MPM-1	77.83	8.86	13.31	3.21	3.27	1.79	0.59	1.83	7.45	4.03
MPM-2	81.71	7.32	10.97	2.80	2.40	1.56	0.56	1.46	5.76	3.75
MPM-4	83.23	5.76	11.01	1.89	1.93	1.47	0.47	1.36	5.84	3.81

Based on the systematic survey of nitrogen- or oxygen-containing carbons, the peaks of the O1s and N1s XPS spectras of various samples are assigned and mass percentage of the different nitrogen/oxygen functionalities was showed in Table 2. Results show that the MPMs contain four types of nitrogen species: pyridinic (N-6), pyrrolic/pyridone (N-5), quaternary nitrogen (N-Q) and pyridine-N-oxide (N-X), and three types of oxygen species: carbonyl oxygen of quinines (OI), carbonyl oxygen atoms in esters, anhydrides and oxygen atoms in hydroxyl groups (OII), non-carbonyl (ether-type) oxygen atoms in esters and anhydrides (OⅢ). Based on previous reports [15, 23], N6, N5, and OI are of electrochemical redox reaction activity, only which can provide the pseudocapacitance. It is supposed that active nitrogen species would dominate the pseudocapacitance since content of active nitrogen is much higher than that of active oxygen. With the increase of R_{MM}, all the active functionalities, including N6, N5 and OI, show remarkable decrease, which indicates that there will be difference in the surface efficiency for different samples.

3.2 Electrochemical properties

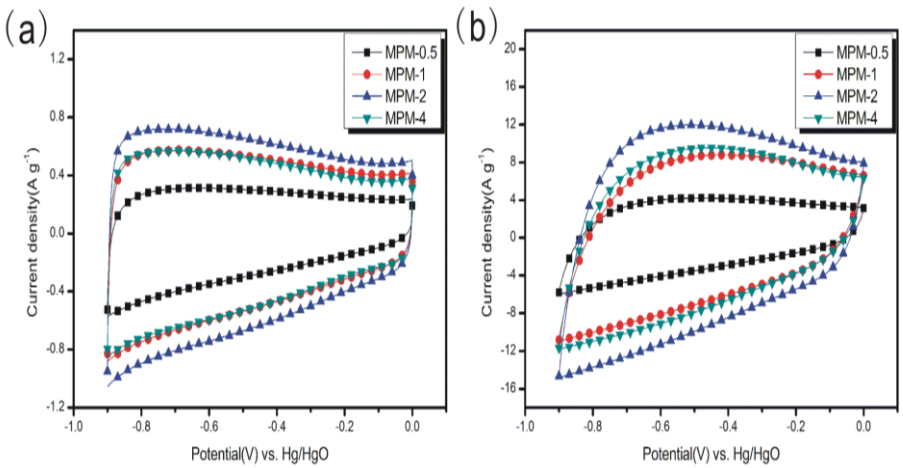

Figure 4. CV curves of samples at scan rate of (a) 5 mV s^{-1}, and (b) 100 mV s^{-1}.

Typical CV curves of MPM-based electrodes were recorded using three-electrode system at different scan rates, and Fig. 4 show the CV curves of samples at scan rate of 5 and 100 mV s^{-1}. It can be seen that the current density, standing for the capacitance, increases gradually with the increase of R_{MM} from 0.5 to 2, and then decreases with the increase of R_{MM} from 2 to 4. Generally, the capacitance is dependent on the BET surface area, but not increases with the surface area linearly [24]. Other factors, such as porous structure, surface functionality and conductivity, also influence the charge propagation. It has been generally reported that it is difficult for electrolyte ions to enter micropores, which yields a low surface utilization ratio. With the highest BET surface area, MPM-4 presents an inferior performance to MPM-2 probably because of lower surface utilization ratio.

As we known, ideal double-layer capacitors are characterized by a perfectly rectangular-shaped CV profile [2]. The deviated CV profiles indicate the presence of redox reactions related to nitrogen- or oxygen-containing functionalities. At low scan rate of 5 mV s^{-1}, current quickly reaches a truly horizontal value after reversal of the potential sweep, resulting in a nearly vertical V/I line. As the scan rate rises to 100 mV s^{-1}, the current response becomes slow, showing a V/I line with a slope. This slope is related to the ion transfer/diffusion behavior [8]. From the CVs at 100 mV s^{-1}, difference can be seen for various samples in the V/I slope. The MPM-0.5 shows the biggest V/I slope, suggesting the slowest ion response. Being deduced by analogy, MPM-2 presents the best ion transfer/diffusion behavior, and next MPM-1, then MPM-4. The results can be explained by the meso/macro-porosity since meso- and macropores provide convenient transfer/diffusion path for electrolyte ions.

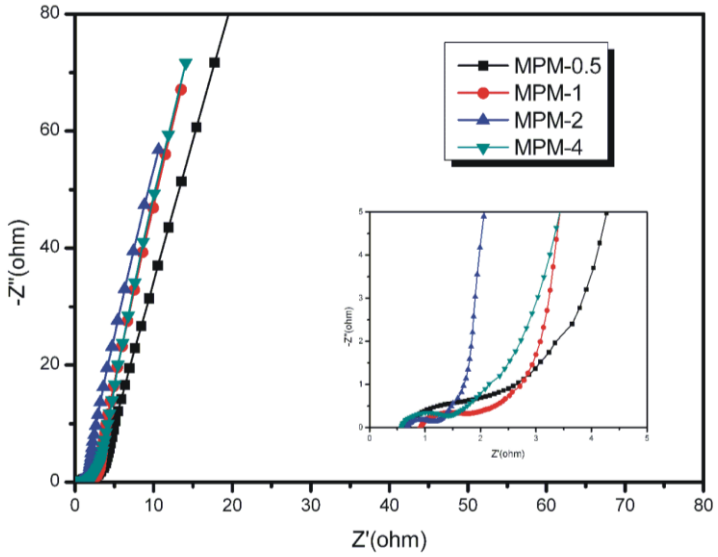

Figure 5. Nyquist plot in the range of 100 kHz-10 mHz.

The ion transfer/diffusion behavior can also be reflected by the ac impedance spectra (Nyquist plot, Fig. 5). It is well known that the ideally polarizable capacitance leads to a straight line along the imaginary axis. However, a real capacitor with a series resistance displays a line with a finite leaning, which stands for the diffusive resistance of the electrolyte ions in the pore of the electrode [25]. The bigger the slope, the lower the diffusive resistance. From the inset in Fig. 5, it can be seen that the order of the slope for various samples is: MPM-2> MPM-1> MPM-4 > MPM-0.5, which means that the order of the ion diffusive rate for various samples is: MPM-2> MPM-1> MPM-4 > MPM-0.5. The result agrees well with that from CVs.

The diameter of the semicircle in the high-frequency region of Nyquist plots stands for the sum of the resistance of the electrode itself and the contact resistance between the electrode and the current collector [25, 26]. Considering that the contact resistance is identical for all samples because of the same cell-assembling technique, this semicircle could be used to assess the intrinsic resistance of active electrode materials. Based on this, it is found that the intrinsic resistance is 1.63Ω for MPM-0.5, decrease to 0.834 Ω for MPM-1 and achieves minimum value of 0.521 Ω for MPM-2, then increases to 0.865 Ω for MPM-4. Generally, for carbon materials, the higher the carbon content, the higher the conductivity. Meanwhile, microstructure, *e.g.* porosity, also plays essential role in the conductivity. A higher porosity would leads to a low conductivity. According to the XPS analysis, with the increase of R_{MM}, the carbon content rises. Hence, the intrinsic resistance keeps decreasing when R_{MM} increases from 0.5 to 2. However, maybe due to the higher porosity, the MPM-4 shows an increased intrinsic resistance.

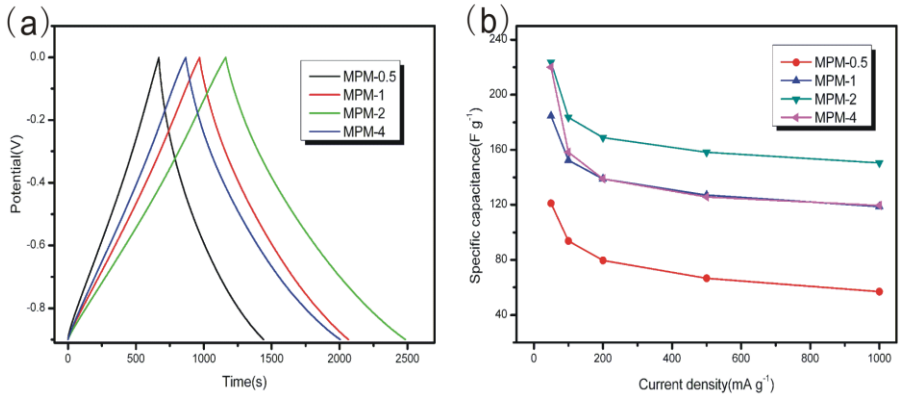

Figure 6. (a) Galvanostatic charge/discharge curves of various samples at current density of 100 mA g^{-1}. (b) Specific capacitance of various samples at various current densities.

To further evaluate the electrochemical performance of the resultant materials, galvanostatic charge/discharge measurements were performed in the potential range from -0.9 to 0 V *vs.* Hg/HgO. Fig. 6a presents charge/discharge curves for all samples at current densities of 100 mA g^{-1}. It can be found that all discharge curves at current density presents a distinct arc shape, even at high current density, which is due to faradic reaction derived from surface functionalities.

The specific capacitance against current density is plotted in Fig. 6b. At current density of 50 mA g^{-1}, MPM-2 has specific capacitance of 224 F g^{-1}, which is even higher than that of some porous carbons with higher surface area, *e. g.* mesoporous carbons with surface area of 720 m^2 g^{-1} show specific capacitance of 179 F g^{-1} [27], nitrogen-enriched multimodal porous carbons with high surface area of 1150 m^2 g^{-1} possess maximal specific capacitance of 177 F g^{-1} [28]. In spite of higher BET surface area, MPM-4 shows much the same specific capacitance (220 F g^{-1}), which may be due to difference in the porous structure and surface chemistry. Limited by relatively low BET surface area, MPM-0.5 and MPM-1 present a lower capacitance, which is 121 and 185 F g^{-1}, respectively.

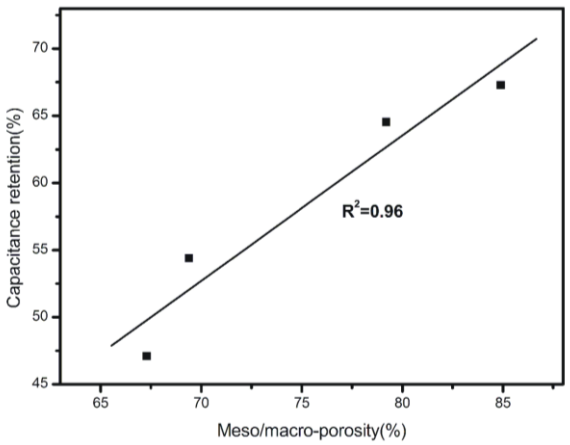

Figure 7. Specific surface capacitance as a function of meso/macro-porosity.

It can be seen that the specific capacitance for all samples decreases with the increase of current density, which is a common phenomenon for porous carbons. Since the diffusion/adsorption of the

ions is limited in the pores, especially in the micropores, charge propagation suffers from an inadequate time at high rate. Generally, the larger the micropore volume, the slower the diffusion/adsorption of the ions, then the bigger the capacitance drop. Due to a large micropores volume (0.113 ml g^{-1}), MPM-4 suffers from the most remarkable capacitance drop of 81 F g^{-1} as the current density increases from 50 to 200 mA g^{-1}. With the smallest micropore volume, MPM-0.5 presents a lowest capacitance drop of 41 F g^{-1} under the same condition. With the current density increasing further to 1000 mA g^{-1}, the capacitance drops are not notable, suggesting capacitive behavior is not ion-diffusion-controlled at this current range. As discussed above, the meso/macro-porosity plays an important role in improving the capacitance retention. This standpoint can be illustrated by plot of capacitance retention *vs.* meso/macro-porosity (as shown in Fig. 7). The capacitance retention increases linearly with the increase of the meso/macro-porosity. MPM-2 presents the higher capacitance retention of 67.3%, owing to its higher meso/macro-porosity of 84.9%.

Table 3. Specific capacitance at current density of 100 mA g^{-1} and specific surface capacitance.

Sample	MPM-0. 5	MPM-1	MPM-2	MPM-4
C (F g^{-1})	121	185	224	220
C_{ssc} (F m^{-2})	2.75	0.88	0.64	0.48

Another important characteristic, noteworthy to mention, is high surface storage efficiency, namely specific surface capacitance (C_{ssc}). Despite moderate specific surface area, these carbons exhibit excellent capacitive performance as compared to previously-reported porous carbons with the same surface area (the specific capacitance is assumed to be less than 100 F g^{-1} for carbons with specific surface area less than 500 m^2 g^{-1} [12]). Generally, the micropores are regarded to be responsible for charge accommodation, whereas the small mesopores can play an adsorption and transporting role. Therefore, increasing of micropore volume is an effective approach to improved C_{ssc}, ignoring the ultra-micropores (< 0.7 nm). However, of the four samples, C_{ssc} decreases with the increase of micropore volume, although all the micropores are ion-accessible [12]. Therefore, it could be speculated that pseudocapacitance related to nitrogen- or oxygen-containing surface functionalities plays a dominant role. Due to the highest nitrogen and oxygen content (9.32 wt.% N and 19.66 wt.% O), MPM-0.5 shows considerable specific capacitance of 121 F g^{-1}, in spite of low BET surface area (44 m^2 g^{-1}). As a consequence, a high C_{ssc} (2.75 F m^{-2}) is obtained, which is in the range of highest ones for reported nitrogen- or oxygen-containing porous carbons (*e. g.*, 0.4 F m^{-2} for N-enriched composite of CNTs [5], 0.11 F m^{-2} for activated and ammoxidized MWCNTs [29], 0.64 F m^{-2} for CNTs/N-enriched carbon [30] and 0.73 F m^{-2} for O-enriched carbons from seaweed polymer [31]). Even with the least nitrogen content, MPM-4 presents a C_{ssc} of 0.48 F m^{-2}, which is also higher than that of conventional porous carbons (0.1~0.15 F m^{-2}) [32].

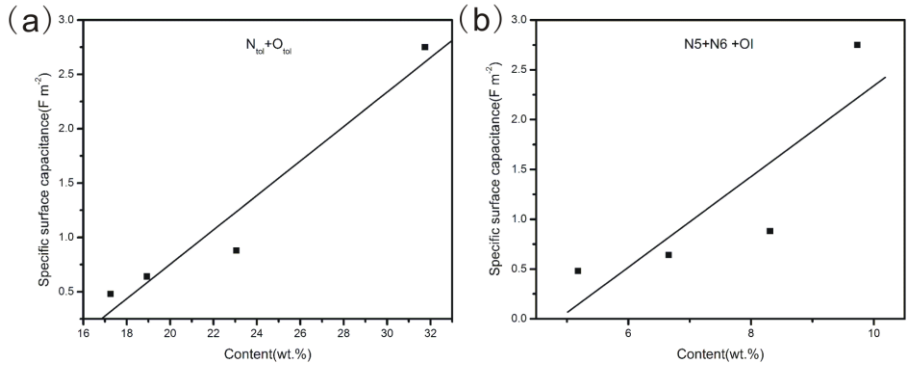

Figure 8. Specific surface capacitance as a function of (a) the sum of N and O and (b) the sum of N5, N6 and OI.

Fig.8 represents the relationship between the C_{ssc} and the content of nitrogen and oxygen species. The C_{ssc} linearly increases with the increase of total content of N and O, confirming the capacitive contribution of the nitrogen and oxygen functionalities, involving increasing electrochemical accessible surface by improving the wettability of the surface and introducing pseudocapacitance derived from electrochemical active functionalities. Furthermore, the C_{ssc} increases with the increase of the sum of N5, N6 and OI, confirming the excellent pseudocapacitance contribution of N5, N6 and OI.

4. CONCLUSIONS

Hierarchical porous carbon with enriched nitrogens was prepared from melamine-formaldehyde resin/poly (vinyl alcohol) blend using MgO as template. The obtained carbons possessed hierarchical porous structure, high meso/macro-porosity (67.3-84.9%) and rich heteroatoms (5.76~9.32 wt.% of N and 10.97~19.66 wt.% of O). Both the porous structure and surface chemistry could be controlled by adjusting the content of template. With the increase of the template, the BET surface area increased and the content of nitrogen and oxygen decreased. Due to the surface functionalities, high specific surface capacitance was achieved. With 9.32 wt.% of N and 19.66 wt.% of O, MPM-0.5 showed a maximal specific surface capacitance of 2.75 F m^{-2}. In addition, meso/macro-porosity played an important role in improving rate performance. With the highest meso/macro-porosity (84.9%) and high content of heteroatoms (7.32 wt.% of N and 10.97 wt.% of O), the sample MPM-2 showed superior electrochemical performance (specific capacitance of 224 F g^{-1}, capacitance retention of 67% and specific surface capacitance of 0.64 F m^{-2}). In summary, this work showed that hierarchical porous carbons with enriched nitrogens exhibit fast ion transportation and excellent pseudocapacitive effect as electrode materials for supercapacitors. Our results provided useful information for expanding the application of porous carbons as electrode materials for supercapacitors.

ACKNOWLEDGEMENTS
This work was financially supported by Natural Science Foundation of China (NO. 50602046), ICC CAS Fund for distinguished Young Scientist, State Education Ministry, Natural Science Foundation of Shanxi Province (NO, 2012011019-3) and 2011 SGL Group Research Assistantship (2011WT906).

References

1. J.R. Miller, P. Simon, *Science* 321 (2008) 651.
2. B.E. Conway, Electrochemical Supercapacitors, Kluwer Academic/Plenum Publishers, New York 1999.
3. A.G. Pandolfo, A.F. Hollenkamp, *J. Power Sources* 157 (2006) 11.
4. E. Frackowiak, F. Béguin, *Carbon* 39 (2001) 937.
5. Q. Li, R. Jiang, Y. Dou, Z. Wu, T. Huang, D. Feng, J. Yang, A. Yu, D. Zhao, *Carbon* 49 (2011) 1248.
6. W. Huang, H. Zhang, Y. Huang, W. Wang, S. Wei, *Carbon* 49 (2011) 838.
7. D.W. Wang, F. Li, M. Liu, G.Q. Lu, H.M. Cheng, *Angew. Chem. Int. Ed.* 120 (2008) 379.
8. F. Xu, R. Cai, Q. Zeng, C. Zou, D. Wu, F. Li, X. Lu, Y. Liang, R. Fu, *J. Mater. Chem.* 21 (2011) 1970.
9. X. Wu, X. Hong, J. Nan, Z. Luo, Q. Zhang, L. Li, H. Chen, *Micropor. Mesopor. Mater*. 160 (2012) 25.
10. Y. Lv, F. Zhang, Y. Dou, Y. Zhai, J. Wang, H. Liu, Y. Xia, B. Tu, D. Zhao, *J. Mater. Chem.* 22 (2012) 93.
11. H. Xu, Q. Gao, H. Guo, H. Wang, *Micropor. Mesopor. Mater*. 133 (2010) 106.
12. L. Zhao, L.Z. Fan, M.Q. Zhou, H. Guan, S.y. Qiao, M. Antonietti, M.-M. Titirici, *Adv. Mater*. 22 (2010) 5202.
13. X. Yang, D. Wu, X. Chen, R. Fu, *J. Phys. Chem.* C 114 (2010) 8581.
14. Y.-R. Dong, N. Nishiyama, M. Kodama, Y. Egashira, K. Ueyama, *Carbon* 47 (2009) 2138.
15. D. Hulicova-Jurcakova, M. Seredych, G.Q. Lu, T.J. Bandosz, *Adv. Funct. Mater*. 19 (2009) 438.
16. E. Frackowiak, G. Lota, J. Machnikowski, C. Vix-Guterl, F. Béguin, *Electrochim. Acta* 51 (2006) 2209.
17. G. Coullerez, D. Léonard, S. Lundmark, H.J. Mathieu, *Surf. Interface. Anal*. 29 (2000) 431.
18. G. Lota, E. Frackowiak, *Fuel Cells* 10 (2010) 848.
19. D. Hulicova-Jurcakova, M. Kodama, S. Shiraishi, H. Hatori, Z.H. Zhu, G.Q. Lu, *Adv. Funct. Mater*. 19 (2009) 1800.
20. H. Konno, H. Onishi, N. Yoshizawa, K. Azumi, *J. Power Sources* 195 (2010) 667.
21. G. Lota, K. Lota, E. Frackowiak, *Electrochem. Commun*. 9 (2007) 1828.
22. Y.J. Kim, Y. Abe, T. Yanagiura, K.C. Park, M. Shimizu, T. Iwazaki, S. Nakagawa, M. Endo, M.S. Dresselhaus, *Carbon* 45 (2007) 2116.
23. K. Jurewicz, R. Pietrzak, P. Nowicki, H. Wachowska, *Electrochim. Acta* 53 (2008) 5469.
24. O. Barbieri, M. Hahn, A. Herzog, R. Kötz, *Carbon* 43 (2005) 1303.
25. K.H. An, W.S. Kim, Y.S. Park, J.M. Moon, D.J. Bae, S.C. Lim, Y.S. Lee, Y.H. Lee, *Adv. Funct. Mater*. 11 (2001) 387.
26. C. Kim, B.T.N. Ngoc, K.S. Yang, M. Kojima, Y.A. Kim, Y.J. Kim, M. Endo, S.C. Yang, *Adv. Mater*. 19 (2007) 2341.
27. L. Li, H. Song, X. Chen, *Electrochim. Acta* 51 (2006) 5715.
28. Y.S. Yun, J. Shim, Y. Tak, H.-J. Jin, *RSC Adv*. 2 (2012) 4353.
29. W. Gao, Y. Wan, Y. Dou, D. Zhao, *Adv. Energy Mater*. 1 (2011) 115.
30. F. Béguin, K. Szostak, G. Lota, E. Frackowiak, *Adv. Mater*. 17 (2005) 2380.
31. E. Raymundo-Piñero, F. Leroux, F. Béguin, *Adv. Mater*. 18 (2006) 1877.
32. M. Inagaki, H. Konno, O. Tanaike, *J. Power Sources* 195 (2010) 7880